Highlights

The study of diffuse interface propagation of dynamic failure in advanced ceramics using the phase-field approach

Benhour Amirian, Bilen Emek Abali, James David Hogan

- Dynamic fracture is modeled by a time-dependent phase-field approach.
- A fully geometrically and physically nonlinear framework is considered for brittle fracture of boron carbide.
- A monolithic scheme is exploited for solving the coupled dynamic equilibrium equation and Ginzburg–Landau equation.

The study of diffuse interface propagation of dynamic failure in advanced ceramics using the phase-field approach

Benhour Amirian[a,*], Bilen Emek Abali[b], James David Hogan[a]

[a] *Department of Mechanical Engineering, University of Alberta, Edmonton, AB T6G 2R3, Canada*
[b] *Department of Materials Science and Engineering, Division of Applied Mechanics, Uppsala University, Box 534, SE-751 21 Uppsala, Sweden*

Abstract

Dynamic failure in advanced brittle materials is a complex mechanical phenomena, which is challenging to study in experimental as well as computational works. This work is set out to model and investigate the crack initiation, growth, propagation, and branching in two-dimensional single crystalline boron carbide at the nanometer length-scale and picosecond time-scale. A phase-field approach is used by carefully selected interfacial energy allowing a monolithic numerical solution method capturing strong coupling between mechanics and damage. Specifically, transient Ginzburg–Landau equation is coupled with the balance of momentum including geometric nonlinearities and solved by using the open-source computing platform FEniCS. The monolithic computation ensures necessary accuracy for dynamic fracture under pure mode I loading and also demonstrates the capability of crack branching depending on the loading rate. The effect of crack regularization length and kinetic coefficient on the crack interface profile and crack tip velocity is also studied. Obtained results are important for modeling anisotropic fracture in advanced ceramics and designing materials with desired characteristics.

Keywords: Dynamic failure, Advanced ceramics, Finite strain, Interface propagation, Phase-field approach;

1. Introduction

Being the most important failure mode in solids and structures, the evolution of cracks as well as their impact on material designs are of great importance to both scientists and

*Corresponding author
Email addresses: benhour@ualberta.ca (Benhour Amirian), bilenemek@abali.org (Bilen Emek Abali), jdhogan@ualberta.ca (James David Hogan)

engineers equally. According to Cox *et al.* [1], all fracture is dynamic at some length-scale and time-scale. Even under quasi-static loading, the crack may propagate at a speed comparable to that of the mechanical waves [2]. Therefore, the unstable propagation of cracks under external dynamic loading necessitates the consideration of inertial effects to analyze the transient behavior of structures or the interactions between stress waves and cracks [3]. Numerous experimental, analytical, and numerical studies have been considered to investigate the dynamic failure of brittle materials. Experimentally, the split-Hopkinson pressure bar systems [4–6], ballistic impact [7], plate impact [8], laser spall [9], laser shock [10], and coupling of real-time visualization techniques (e.g., ultra high-speed imaging) with laboratory-based experiments [11] have been employed to probe the fracture behavior of advanced ceramics during dynamic loading; however, the energy flux to the crack tip and its connection to the crack velocity, as one of the main difficulty in the theory of high speed dynamic crack propagation, cannot directly be measured from experimental tests [12].

Atomistic simulations, largely represented by molecular dynamics (MD) simulations and density functional theory (DFT), are the bridge between continuum and atomic description of dynamic fracture. Examples are the method of lattice dynamics modeling [13] and tight binding methods [14]. Despite having successful connection between atomistic approaches and continuum-scale theory and experimentation [15], these atomistic viewpoints often suffers from limitation of modeling time, which leads to a loading rate much higher than the rate of practical interest [16], and are forbiddingly expensive if extended to realistic length scales [17].

Among the theoretical studies for understanding the underlying physics and mechanics of dynamic fracture [18, 19], the Griffith criterion was one of the earliest description which was based on an energy balance equation [20]; however, practical engineering examples are usually too complex to be solved using analytical techniques. Therefore, numerical methods play a vital role in dynamic failure. For example, discrete crack models, such as the discrete element method [21, 22], the extended finite element method (XFEM) [23–25], the cohesive zone method [26], and the cohesive segment method [27], allow the displacement field to be discontinuous across the fracture surfaces. Regardless of showing much success in modeling crack propagation [28], the discrete crack models need additional energy-based criteria to simulate the dynamic fracture problems [29, 30]. In addition, the discrete crack model requires remeshing algorithms or using the partition of unity method [31], both having

their own difficulties in tracking the multiple crack fronts in complex three dimensional morphologies [32, 33]. In the smeared (continuum) crack model, including the gradient damage model [34, 35] and diffuse interface models [36–40], the displacement is continuous everywhere and stresses gradually decrease to model the degradation process. The coupling of discrete and smeared crack approaches (e.g., the element deletion method [41] and the thick level-set method [42]) have also shown promising results in modeling fracture. However, there are drawbacks as the dependence of the results on the finite element meshes and the convergence path of the solutions results in numerical errors [43].

The phase-field model is an alternative approach that has been successfully adopted in the simulation of martensitic phase transformations [44], melting [45], dislocations [46], twinning [47], fracture [48–56], and their interactions [57–60]. One of the main advantages of the phase-field approach to study the failure mechanisms in brittle materials over the previous methods is predicting the evolution of interfaces (e.g., merging and branching of multiple cracks) with no additional effort [61–63], making phase-field modeling a powerful and flexible method for studying the fracture of single-crystalline [64, 65], polycrystalline [66], and granular materials [67]. In the physics community, the phase-field models are commonly derived by adapting the phase transition formalism of Landau and Ginzburg [68] to study the dynamic crack propagation in brittle solids [69, 70]. The advantage of the Ginzburg–Landau approach over the incremental energy minimization method [64] is that material parameters associated with time scales for interfacial motion enter the model, making it a more general model for studying the dynamic failure of highly brittle materials.

Numerically, the coupled nonlinear equilibrium and the Ginzburg–Landau equations are solved via a staggered or monolithic scheme. The former is based on decoupling balance equations and the phase-field problem into the system of two equations that are solved in a subsequent manner [71, 72]. Giving rise to two convex minimization problems, the method is robust; however, a significant amount of staggered iterations may be required at a fixed loading step, resulting in a higher computational cost [73]. In the monolithic scheme, all solution variables are solved simultaneously [74] that is more efficient for strongly coupled systems of equations as a result of less Newton–Raphson iterations [75].

The current paper extends the Ginzburg–Landau phase-field approach to predict dynamic fracture in single crystal boron carbide (B_4C) under mode I loading. In addition, the focus of this work is on derivation of governing equations and solving them monolithically

in order to increase the accuracy for applications with strong coupling between mechanics and damage growth. Governing equation for the phase-field method is motivated differently than balance equations and there is a computational difficulty to implement monolithic schemes. Hence, the literature lacks studies focused on solving the Ginzburg–Landau based phase-field problem for predicting the dynamic crack branching of brittle materials by using a monolithic scheme. By following the works on local stress concentrations in nanoscale defect-free volumes or by high pressures [76], we develop a highly nonlinear phase-field theory for elasticity along with anisotropic surface energy [77]. In this way, numerical problems are circumvented owing to governing equations motivated by thermodynamics and we manage to solve these nonlinear and coupled differential equations by exploiting the open-source parallel computing platform FEniCS [78, 79].

The remainder of this paper is outlined as follows. In Section 2, we present continuum mechanics and thermodynamically sound derivation of equations and their variational formulation for the finite element method. Then in Section 3, results and representative material properties are reported along with the discussion of phase-field simulations. The conclusions of the study are drawn in Section 4.

2. Governing equations

We describe a model for a single fracture system in solids based on thermodynamical derivations. The present approach accounts for the time-evolution of the fracture order (or damage) parameter toward an equilibrium state for predicting the crack paths in anisotropic single crystal materials adequately. This allows the study of spatio-temporal fluctuations of damage variables, as well as the nanoscale dynamics that govern various pattern forming phenomena [80, 81]. Moreover, the interfaces, their propagation, and interactions, which are the most important features governing the formation of microstructures in materials [82–85], is studied via this newly implemented approach.

2.1. Material

As a result of possessing hardness above 30 GPa, low mass density ($2.52\,\mathrm{g/cm^3}$), and high Hugoniot elastic limit (17 -20 GPa), boron carbide (B_4C) has received considerable attention in ballistic applications [86]. Due to its high melting point and thermal stability [87], extreme abrasion resistance [88], and high temperature semiconductivity [89], boron carbide is

widely used in refractory, nuclear, and novel electronic applications, respectively; however, its performance is hindered by one or more of a number of inelastic deformation mechanisms, including deformation twinning [90], stress-induced phase transformations [91, 92], and various anisotropic fracture behaviors [93] when subjected to mechanical stresses exceeding their elastic limit. In the literature, the key failure mechanisms in boron carbide (e.g., cleavage fracture and twinning) are commonly studied experimentally using numerous characterization techniques (e.g., transmission electron microscopy [94] and Raman spectroscopy [95]). Fracture in the form of shear failure, cavitation, and cleavage has been confirmed from atomic simulation results, either via first principles or molecular dynamics simulations [96, 97]. Finite deformation continuum models, such as cohesive zone models for fracture [98] and crystal plasticity [99] have also been used to investigate inelastic deformation in single and polycrystalline boron carbide. The present time-evolved phase-field model seeks to engineer the next generation of anisotropic boron carbide-based ceramics by understanding the important plastic deformation and brittle fracture mechanisms that govern its high rate performance.

2.2. Order parameter

The main desired feature of the proposed model is to introduce an order parameter η assigned to each material point $\boldsymbol{X}$ to represent fracture, where $\eta = 0$ indicates undamaged material, $\eta = 1$ fully damaged material, and $\eta \in (0, 1)$ partially degraded material. This variable is commonly assumed to be at least $\mathcal{C}^2$-continuous with respect to $\boldsymbol{X}$ according to the diffuse interface theory [100, 101].

2.3. Kinematics

We use standard continuum mechanics notation and understand a summation over repeated indices. The reference, stress-relaxed intermediate, and current configurations are denoted by $\mathfrak{B}_0$, $\mathfrak{B}_t$, and $\mathfrak{B}$, respectively. For the balance of momentum, the computational domain will be $\mathfrak{B}_0$ with its closure $\partial\mathfrak{B}_0$. On Neumann boundaries, $\partial\mathfrak{B}_{0_{\mathcal{N}i}}$, gradient of the solution is known by the given traction vector and on Dirichlet boundaries, $\partial\mathfrak{B}_{0_{\mathcal{D}i}}$, the solution itself (displacement) is given. The motion from the reference position $\boldsymbol{X}$ to the current (deformed) position $\boldsymbol{x} = \boldsymbol{X} + \boldsymbol{u}$ is given by the displacement tensor of rank one, $\boldsymbol{u} = \boldsymbol{u}(\boldsymbol{X}, t)$, as a function in space, $\boldsymbol{X}$, and time, t. The deformation gradient, $\boldsymbol{F} = \nabla\boldsymbol{x}$, is a compatible

($\nabla \times \boldsymbol{F} = 0$) non-singular two-point tensor; ∇ is the gradient operator in the undeformed state. The right Cauchy–Green deformation tensor and the Jacobian determinant read

$$\boldsymbol{C} = \boldsymbol{F}^{\mathsf{T}} \cdot \boldsymbol{F}, \quad J = \det(\boldsymbol{F}), \tag{1}$$

respectively. Then the strain measure is nonlinear, called Green–Lagrange strain tensor, as follows:

$$\boldsymbol{E} = \frac{1}{2}(\boldsymbol{C} - \boldsymbol{I}). \tag{2}$$

Therefore, we model the geometric nonlinearities accurately. Even if the material model is elastic, the governing equation is nonlinear. The interpolation function $\phi(\eta)$ is obtained from a general representative function $\varphi(a, \eta)$ as a fourth-degree potential [102] defined as

$$\varphi(a, \eta) = a\eta^2(1 - \eta)^2 + \eta^3(4 - 3\eta), \tag{3}$$

where a is a constant parameter—in order to ensure that $\varphi(a, \eta)$ is a monotonous function, a is chosen between 0 and 6. The interpolation function $\varphi(a, \eta)$ satisfies the conditions

$$\varphi(a, 0) = 0, \ \varphi(a, 1) = 1, \ \frac{\partial \varphi(a, 0)}{\partial \eta} = \frac{\partial \varphi(a, 1)}{\partial \eta} = 0. \tag{4}$$

2.4. Free energy and dissipation inequality

The dissipation inequality is derived by following thermodynamics of irreversible phenomena [103]. Considering the balance of energy and subtracting the balance of kinetic energy constructed from the balance of momentum, we obtain the balance of internal energy for each material point as

$$\rho_0 \dot{U} + \nabla \cdot \boldsymbol{Q} - \rho_0 r = \boldsymbol{P} : \dot{\boldsymbol{F}}^{\mathsf{T}}. \tag{5}$$

Here, ρ_0 is the mass density in the initial configuration, U is the specific (per unit mass) internal energy, $\boldsymbol{Q}$ is the (heat) flux term across the orthogonal direction, r is the (known) specific volumetric heat supply rate per unit mass, the right-hand side, $\boldsymbol{P} : \dot{\boldsymbol{F}}^{\mathsf{T}}$, is a production term, and $\boldsymbol{P}$ is the Piola stress (first Piola–Kirchhoff stress tensor). We begin with a rather general model and define entropy flux as the heat flux times inverse of temperature, T, as well as entropy supply term as the internal energy supply term multiplied by $1/T$.

Hence, we obtain the balance of entropy:

$$\rho_0 \dot{s} + \nabla \cdot \frac{1}{T}\boldsymbol{Q} - \frac{1}{T}\rho_0 r = \rho_0 \Sigma, \tag{6}$$

where specific (per mass) entropy, s, and the entropy production, Σ, need to be defined. The second law of thermodynamics asserts that the entropy production is zero for reversible and positive for irreversible processes. By replacing the supply term in Eq. (5) and using divergence theorem, we obtain

$$\boldsymbol{P} : \dot{\boldsymbol{F}}^{\mathsf{T}} - \rho_0 \dot{U} + \rho_0 T \dot{s} - \frac{\nabla T}{T} \cdot \boldsymbol{Q} \geq 0. \tag{7}$$

If we model the heat flux by the Fourier's law

$$\boldsymbol{Q} = -\boldsymbol{\kappa}_T \cdot \nabla T, \tag{8}$$

where $\boldsymbol{\kappa}_T$ is the positive-definite heat conductivity tensor, entropy production's last term is always positive—we emphasize that T is in kelvin. By substituting U with the specific Helmholtz free energy, $\psi = U - Ts$ and assuming that the heat conduction and other thermo-mechanical processes are mutually independent [104], the mechanical dissipation inequality reads

$$\boldsymbol{P} : \dot{\boldsymbol{F}}^{\mathsf{T}} - \rho_0 \dot{\psi} - \rho_0 \dot{T} s \geq 0. \tag{9}$$

In thermoelasticity, the free energy does depend on strain and temperature. Now we extend the model for the free energy in such a way that the phase-field approach is acquired. We prescribe the constitutive relation for ψ by assuming dependency also on the fracture order parameter, η, and its first derivative, $\nabla\eta$. Substituting $\dot{\psi}$ into Eq. (9), using an integration by parts, and regrouping by means of variables in the energy $\boldsymbol{F}$, T, η, $\nabla\eta$, we obtain

$$\left(\boldsymbol{P} - \rho_0 \frac{\partial \psi}{\partial \boldsymbol{F}}\right) : \dot{\boldsymbol{F}}^{\mathsf{T}} - \rho_0 \left(s + \frac{\partial \psi}{\partial T}\right) \dot{T} + \rho_0 \left(\nabla \cdot \frac{\partial \psi}{\partial \nabla \eta} - \frac{\partial \psi}{\partial \eta}\right) \dot{\eta} \geq 0. \tag{10}$$

Since this inequality holds for every process, we conclude to these constitutive equations for reversible processes generating zero entropy production,

$$\boldsymbol{P} = \rho_0 \frac{\partial \psi}{\partial \boldsymbol{F}}, \;\; s = -\frac{\partial \psi}{\partial T} \; . \tag{11}$$

We may write the inequality,

$$\rho_0 \mathcal{X} \dot{\eta} \geq 0, \tag{12}$$

with a so-called thremodynamic flux, $\rho_0 \mathcal{X}$, conjugate to a so-called thermodynamic force, $\dot{\eta}$. Hence, we model the thermodynamic flux depending on the thermodynamic force in such a way that their multiplication remains positive. Therefore, this model is for irreversible processes. The simplest model is a linear one,

$$\dot{\eta} = \rho_0 \mathcal{L}^{\eta} \left(\nabla \cdot \left(\frac{\partial \psi}{\partial \nabla \eta} \right) - \frac{\partial \psi}{\partial \eta} \right) , \tag{13}$$

by choosing a constant (mobility) parameter $\mathcal{L}^{\eta}$, which is also called the Ginzburg–Landau (evolution) equation. Indeed, $\mathcal{L}^{\eta}$ is a positive (kinetic) coefficient steering an energy dissipation in the form of heat during the crack propagation [36].

2.5. Governing equations

According to the strength and fracture toughness of B_4C being constant from room temperature to 1500 K [105], an isothermal process is assumed. Therefore, we aim for solving the balance of momentum and evolution equation for the phase-field (order) parameter. Also, we emphasize that the model of the system accounts for inertial effects, since it is essential for modeling unstable crack propagation in brittle materials [106]. We neglect the deformation due to weight and set the gravitational body force to zero. In other words, for an isothermal, dynamic case, the deformation is caused by the mechanical loading on boundaries such that the governing equations become

$$\begin{aligned} \rho_0 u_i^{\bullet\bullet} &= P_{ji,j} \, , \;\; P_{ji} = \rho_0 \frac{\partial \psi}{\partial F_{ij}} \, , \\ \frac{1}{\mathcal{L}^{\eta}} \eta^{\bullet} &= - \rho_0 \frac{\partial \psi}{\partial \eta} + \rho_0 \Big(\frac{\partial \psi}{\partial \eta_{,i}} \Big)_{,i} \, , \end{aligned} \tag{14}$$

where displacement, $\boldsymbol{u}$, and phase-field, η, are unknowns to be solved. We stress that the whole formulation is acquired by choosing the Helmholtz free energy adequately. We propose to use the following free energy:

$$\psi(\boldsymbol{F}, \eta, \nabla \eta) = g(\eta) \psi^{\mathrm{e}}(\boldsymbol{F}) + \psi^{\nabla}(\eta, \nabla \eta) \, , \tag{15}$$

where $g(\eta)$ is the degradation function, ψ^e and ψ^∇ are the mechanical energy and interfacial energy per unit mass, respectively. The degradation function indicates that the mechanical energy of the structure at each position degrades by the order parameter

$$g(\eta) = \zeta + (1-\zeta)\,(1-\eta)^2\,. \tag{16}$$

The constant ζ ensures a minimal residual stiffness for fully fractured materials. The quadratic degradation of elastic energy has likewise been used in a number of other phase-field and gradient damage models [34, 107]. For the elastic strain energy density in the initial configuration, we use a quadratic energy description leading to a linear material model,

$$\rho_0 \psi^{\mathrm{e}} = \frac{1}{2} E_{ij} C_{ijkl} E_{kl}. \tag{17}$$

The fourth-order stiffness tensor, $\boldsymbol{C}$, depends on the elasticity tensor of the perfect (virgin, without damage) material $\boldsymbol{C}(\eta = 0)$ and the fracture order parameter η as

$$\boldsymbol{C} = g(\eta)\boldsymbol{C}(\eta = 0)\ . \tag{18}$$

For the interfacial energy density W^∇, the following decomposition is used

$$W^\nabla(\eta, \nabla\eta) = W_1^\nabla(\eta) + W_2^\nabla(\nabla\eta). \tag{19}$$

For cleavage fracture, which is the primary failure mode in boron carbide, we choose the terms in Eq. (19) as follows:

$$\begin{aligned} W_1^\nabla(\eta) =& \mathcal{B}\eta^2, \\ W_2^\nabla(\nabla\eta) =& \omega_{ij}\eta_{,i}\eta_{,j},\ \omega_{ij} = \omega_0\big(\delta_{ij} + \beta(\delta_{ij} - M_i M_j)\big), \end{aligned} \tag{20}$$

where $\mathcal{B} = \Upsilon/l$ is the ratio of fracture surface energy Υ and crack thickness or regularization length l, $\omega_0 = \Upsilon l$ is a material constant, β is the cleavage anisotropy factor, and $\boldsymbol{M}$ is the orientation of the cleavage plane, which is known a priori [71, 72]. The cleavage plane can be a plane of low surface energy or low intrinsic strength in the crystal [108]. The parameter β penalizes fracture on planes not normal to $\boldsymbol{M}$ so that $\beta = 0$ results in isotropic damage.

The regularization length is taken as the cohesive process zone for shear failure [109]

$$l = \frac{16\pi\Upsilon}{\mu_0\,(1-\nu_0)}, \tag{21}$$

where $\mu_0/2\pi$ is the theoretical shear failure strength, and $\nu_0 = {}^{(3k_0-2\mu_0)}/_{(6k_0+2\mu_0)}$ [110].

By using the aforementioned material modeling and strain definition in Eq. (17), the governing equations (14) read for displacement

$$\rho_0 \ddot{u_i} = P_{ji,j}\ ,\ P_{ji} = g(\eta)\frac{\partial \psi^{\mathrm{e}}}{\partial F_{ij}} = g(\eta)\frac{\partial \psi^{\mathrm{e}}}{\partial E_{kl}}\frac{\partial E_{kl}}{\partial F_{ij}}. \tag{22}$$

with

$$\begin{aligned} \frac{\partial \psi^{\mathrm{e}}}{\partial E_{kl}} =& S_{kl} = C_{klij}E_{ij}\ ,\ S_{kl} = S_{lk}\ , \\ \frac{\partial E_{kl}}{\partial F_{ij}} =& \frac{1}{2}\frac{\partial}{\partial F_{ij}}\left(F_{pk}Fpl - \delta_{kl}\right) = \frac{1}{2}\left(\delta_{pi}\delta_{kj}F_{pl} + F_{pk}\delta_{pi}\delta_{lj}\right)\ . \end{aligned} \tag{23}$$

For the phase-field, in the case of a homogeneous material $\rho_0 = \text{const.}|_{\boldsymbol{X}}$, we have

$$\begin{aligned} \frac{1}{\mathcal{L}^{\eta}}\dot{\eta} =& -\rho_0\frac{\partial \psi}{\partial \eta} + \rho_0\Big(\frac{\partial \psi}{\partial \eta_{,i}}\Big)_{,i} = -g'(\eta)\psi^{\mathrm{e}} - \frac{\partial W_1^{\nabla}}{\partial \eta} + \Big(\frac{\partial W_2^{\nabla}}{\partial \eta_{,i}}\Big)_{,i} \\ =& -\frac{1}{2}g'(\eta)E_{ij}C_{ijkl}E_{kl} - 2\mathcal{B}\eta + \Big(2\omega_0\big(\delta_{ij} + \beta(\delta_{ij} - M_iM_j)\big)\eta_{,j}\Big)_{,i}\ . \end{aligned} \tag{24}$$

To satisfy the antisymmetry condition for the interpolation function $\phi(\eta)$, we use Eq. (4) by setting $a = 3$ and obtain

$$\phi(\eta) = \varphi(3,\eta) = 3\eta^2 - 2\eta^3 + \eta^4\ . \tag{25}$$

2.6. Variational formulation

Governing equations are replaced by their weak forms and we follow the standard techniques, so-called variational formulation for generating weak forms and then solve them numerically by means of the finite element method [111]. The space discretization is incorporated by approximating fields, $\boldsymbol{u}$ and η, by spanning over nodal values after a triangulation of the computational domain, Ω, with its closure, $\partial\Omega$, into finite elements. For the sake of a simpler notation, we skip a notational change for approximated fields, since their analytical and discrete representations never occur in the same formulation. We emphasize that all unknowns, $\{\boldsymbol{u}, \eta\}$, are solved in a monolithic manner, therefore, the Hilbertian–Sobolev

space, $\mathcal{H}^1$, on a triangulation τ, as follows:

$$\begin{aligned}\mathcal{V} = \Bigg\{ & \left\{\boldsymbol{u}\right\} \in \mathcal{H}^1(\Omega) : \left\{\boldsymbol{u}\right\}\Big|_\tau \mathcal{P}_a(\tau) \ \forall \tau \in \mathcal{T} \\ & \wedge \left\{\eta\right\} \in \mathcal{H}^1(\Omega) : \left\{\eta\right\}\Big|_\tau \mathcal{P}_b(\tau) \ \forall \tau \in \mathcal{T} \Bigg\} \ .\end{aligned} \tag{26}$$

We use a discretization using Lagrange elements and generate piecewise continuous polynomials that are adequate for approximation in $\mathcal{H}^1$. This triangulation is denoted $\mathcal{T}$ and consists of non-overlapping triangles, τ. This standard FEM elements are of order $a = 2$ and $b = 1$ such that we use linear elements for the phase-field and quadratic elements for displacement. As is common in the Galerkin approach, the same space from above is used in defining test functions,

$$\begin{aligned}\bar{\mathcal{V}} = \Bigg\{ & \left\{\delta\boldsymbol{u}\right\} \in \mathcal{H}^1(\Omega) : \left\{\delta\boldsymbol{u}\right\}\Big|_\tau \mathcal{P}_a(\tau) \ \forall \tau \in \mathcal{T} \\ & \wedge \left\{\delta\eta\right\} \in \mathcal{H}^1(\Omega) : \left\{\delta\eta\right\}\Big|_\tau \mathcal{P}_b(\tau) \ \forall \tau \in \mathcal{T} \Bigg\} \ .\end{aligned} \tag{27}$$

For the time discretization, we use a Euler backwards scheme for the order parameter and velocity, for example for the current unknown value, $\eta = \eta(t)$, we utilize the solution from one time step before, $\eta^0 = \eta(t - \Delta t)$, and hence

$$\eta^{\bullet} = \frac{\eta - \eta^0}{\Delta t} \ . \tag{28}$$

We use a constant time step, Δt. Multiplying governing equations by test functions, generating integral forms, and then integrating by parts where necessary, we obtain

$$\text{Form}_{\boldsymbol{u}} = \int_\Omega \left(\rho \frac{u_i - 2u_i^0 + u_i^{00}}{\Delta t \Delta t} - P_{ji}\delta u_{i,j} \right) \mathrm{d}V + \int_{\partial\Omega_\mathrm{N}} \hat{t}_i \delta u_i \, \mathrm{d}A \ , \tag{29}$$

where a traction vector, $\hat{\boldsymbol{t}}$, is given on Neumann boundaries, $\partial\Omega_\mathrm{N}$. Analogously, we construct a weak form for the phase-field governing equation, where we use integration by parts only

for the second derivative in η term,

$$\begin{aligned}\mathrm{Form}_\eta = \int_\Omega \Bigg(& \frac{\eta - \eta^0}{\mathcal{L}^\eta \Delta t}\delta\eta + \frac{1}{2}g'(\eta)E_{ij}C_{ijkl}E_{kl}\delta\eta + 2\mathcal{B}\eta\delta\eta \\ & + 2\omega_0\big(\delta_{ij} + \beta(\delta_{ij} - M_i M_j)\big)\eta_{,j}\delta\eta_{,i}\Bigg)\,\mathrm{d}V \ .\end{aligned} \tag{30}$$

The implementation solves the nonlinear weak form

$$\mathrm{F} = \mathrm{Form}_{\boldsymbol{u}} + \mathrm{Form}_\eta \ . \tag{31}$$

The solution method is based on a Newton–Raphson solver. In each iteration, the weak form depending on unknowns, $\boldsymbol{P} = \{\boldsymbol{u}, \eta\}$, and their corresponding test functions, $\delta\boldsymbol{P} = \{\delta\boldsymbol{u}, \delta\eta\}$, is linearized by an expansion around the unknowns from the last iteration, $\boldsymbol{P}$, in order to calculate $\boldsymbol{P} + \Delta\boldsymbol{P}$. Indeed, the solution is for the increment, $\Delta\boldsymbol{P}$, where the problem is linear by cutting the expansion at second order terms

$$F(\boldsymbol{P} + \Delta\boldsymbol{P}, \delta\boldsymbol{P}) = F(\boldsymbol{P}, \delta\boldsymbol{P}) + \nabla_{\boldsymbol{P}} F(\boldsymbol{P}, \delta\boldsymbol{P}) \cdot \Delta\boldsymbol{P} \ , \tag{32}$$

where the derivative in unknowns is established by Gateaux (or directional) derivative:

$$\nabla_{\boldsymbol{P}} F(\boldsymbol{P}, \delta\boldsymbol{P}) \cdot \boldsymbol{P} = \lim_{\epsilon \to 0} \frac{\mathrm{d}}{\mathrm{d}\epsilon} F(\boldsymbol{P} + \epsilon\Delta\boldsymbol{P}, \delta\boldsymbol{P}) \ . \tag{33}$$

This standard formulation is beneficial but cumbersome for implementation if the latter derivative is determined manually. Therefore, on a higher level, we use open-source packages from SyFi in FEniCS [112, 113] allowing to obtain this part via the symbolic derivative such that the weak form's nonlinearity may be as complicated as it gets, yet the implementation remains the same.

3. Numerical simulations demonstrating the instability of a tensile loaded fast moving crack in a single crystal boron carbide

The weak forms in Eq. (31) are nonlinear and coupled. We present a monolithic implementation of this transient, fully coupled system of equations by using open-source packages from the FEniCS Project [114]. We emphasize that the literature is often suggesting a

staggered scheme, see for example [115–117] for implementations in FEniCS. The staggered solution solves many smaller problems than one larger, which is faster since the computational cost increases exponentially [118, 119]. However, in a staggered algorithm, several iterations are necessary for solving one time step in order to ensure that coupling between unknowns is fulfilled with the chosen accuracy. Generally speaking, for highly-coupled systems, a monolithic approach is more feasible. Herein, the implementation is using a monolithic approach, where displacement and phase fields are solved at once. As aforementioned, the linearization is done automatically by means of a symbolic derivation which is proven to be more reliable [120, 121]. The conjugate gradient method with a Jacobi preconditioner from PETSc packages has been employed for solving the nonlinear equations. The simulation has been performed by a computing node using Intel Xeon E7-4850, in total 64 cores each with the 40 MB cache, equipped with 256 GB Memory in total, running Linux Kernel 5 Ubuntu 20.04. The code is written in Python, although the FEniCS software wraps the formulation to a C++ code and solves as a compiled program. Therefore, yet efficient in developing the code, all computation is running in parallel such that large scale problems are possible to solve.

A popular 2-D example under different loading conditions is demonstrated next in order to simulate unstable crack propagation observed in ceramic boron carbide. The results are adequate, qualitatively and quantitatively. The material properties used in the simulations are shown in Table 1 for B_4C.

For the example below, the mesh size, h, is such that 10 elements are considered at the interface to resolve the sharp variation along the interface width. Experience has shown that this size provides sufficient accuracy without over resolving the crack. Analysis of the computational solution of this example improves understanding a rapid failure at length- and time-scales not feasible to demonstrate experimentally. These extreme conditions are so challenging to detect experimentally, we must rely on accurate multiphysics simulations. Hence, we stress the importance of the choice of a monolithic solution strategy.

In this example, we model a pre-notched rectangular plate loaded dynamically in tension. This phenomena has been extensively studied by experimental approaches [126, 127]. Regarding phase-field models, the Mode I branching problem has been treated in Borden *et al.* [40] and Bleyer *et al.* [128]. Both investigations used the small strain framework for precisely locating when and where branching occurs; however, the material is exposed to

Table 1: Material properties and model constants for B_4C

Parameters	Notation	Value	Reference
Elastic constants	$C_{11} =$	487 GPa	[122, 123]
	$C_{12} =$	117 GPa	
	$C_{13} =$	66 GPa	
	$C_{33} =$	525 GPa	
	$C_{44} =$	133 GPa	
Initial shear modulus	$\mu_0 =$	193 GPa	[124]
Initial bulk modulus	$k_0 =$	237 GPa	
Density	$\rho =$	2520 $^{\text{kg}}/_{\text{m}^3}$	[124]
Cleavage anisotropy factor	$\beta =$	$0 - 100$	[124]
Fracture surface energy	$\Upsilon =$	3.27 $^{\text{J}}/_{\text{m}^2}$	[125]
Regularization length	$l =$	1.04 nm	Eq. (21)

large strain before and during fracture at the nanoscale [129]. The geometry and loading conditions are depicted in Figure 1.

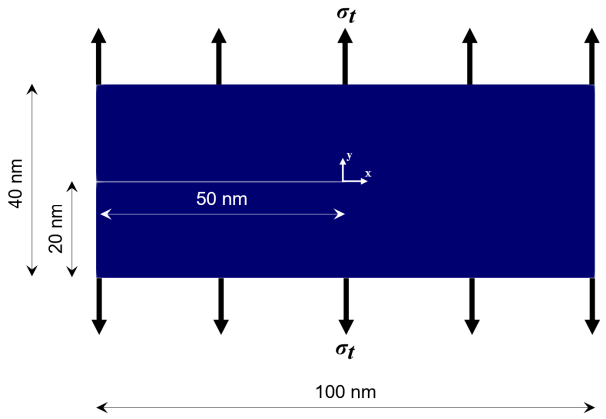

Figure 1: The geometry and boundary conditions for the dynamic crack branching example. The specimen contains a crack and is subjected to a symmetric traction load.

The phase-field (order parameter) distribution along x-axis in Fig. 1 is illustrated in Fig. 2. Mechanical loading of amplitude σ_t is established by a traction vector vertical to top and bottom boundaries, $\sigma_t \boldsymbol{n}$, where $\boldsymbol{n}$ is the surface normal outward the continuum body. This traction is applied at the initial time step and held constant throughout the simulation. We investigate three cases with the amplitude chosen as 1.5 GPa, 1.7 GPa, and 1.9 GPa. The regularization length is $l = 0.5$ nm, and plane strain is assumed. The highlighted region

shows that the fracture order parameter's value is increasing until reaching to the final value $\eta = 1$, where the actual crack tip (where $\eta = 1$) forms at $t = 1.3\,\text{ps}$ and after that the crack starts to grow and propagate along the crack length.

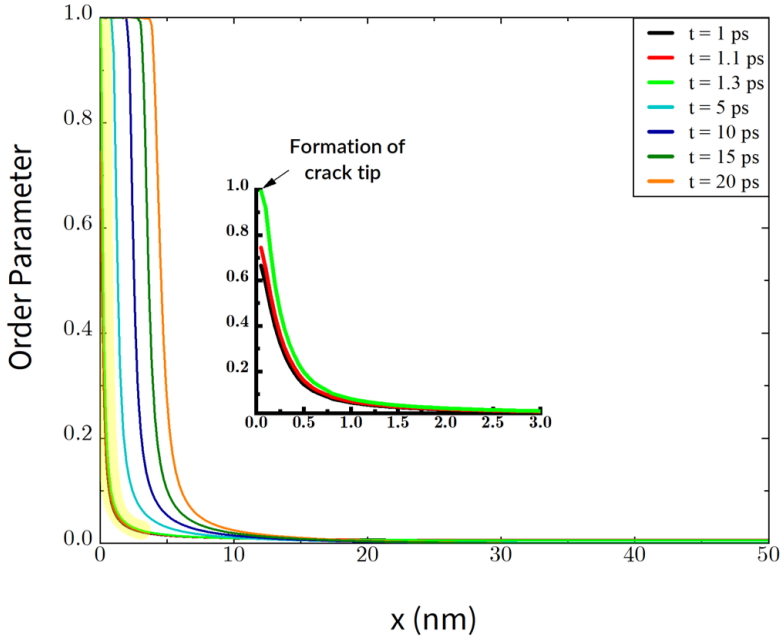

Figure 2: The dynamic crack profiles versus the crack notch's length x at different time steps for regularization length of $l = 0.5\,\text{nm}$ under a uniaxial tension stress of $\sigma_t = 1.5\,\text{GPa}$. The inset shows the highlighted order parameter's distribution in yellow for $t = 1\,\text{ps}$, $1.1\,\text{ps}$, and $t = 1.3\,\text{ps}$.

Next, distribution of the phase-field (damage) is analyzed. At different time steps, along different vertical slices, under the same loading scenario, we plot the damage field, η, in Fig. 3. The kinetic coefficient parameter used in the phase-field model, which is unknown for boron carbide, is assumed to be $\mathcal{L} = 1000\,\text{Pa}^{-1}\,\text{s}^{-1}$ and the crack regularization length is $l = 0.5\,\text{nm}$. Under the loading $\sigma_t = 1.5\,\text{GPa}$, at $x = 1\,\text{nm}$ distance from the notch tip, the vertical distribution of damage in Fig. 3(a) provides an insight that the crack reaches this distance between $5\,\text{ps}$ and $10\,\text{ps}$. Also, there is a small plateau for the interface profile at $t = 22\,\text{ps}$ which is related to a small deviation of the crack path. At $x = 2\,\text{nm}$, the interface profiles demonstrate the motion of the crack more clearly. By moving through the length of the specimen, $x = 4\,\text{nm}$, it is clear that the crack thickness also increases by comparing the distance between every two points on order parameter profiles at each time step in Fig. 3(d). In addition, there is a small drop in the peak point of damage variable at $t = 22\,\text{ps}$ which shows the existence of branching.

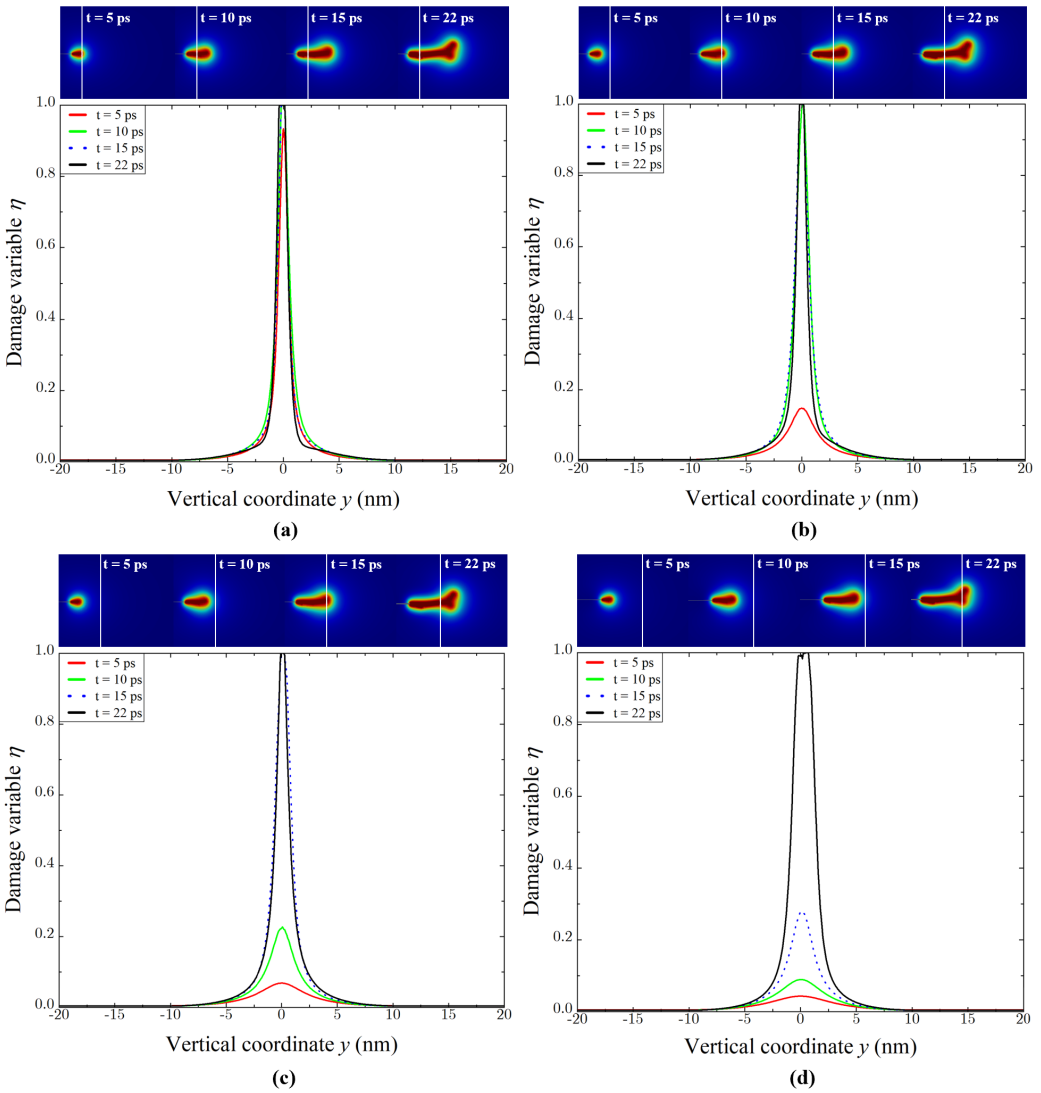

Figure 3: Symmetric damage interfaces under a uniaxial tension stress of 1.5 GPa at different time steps along different vertical slices $\{(x, y) \in \mathbb{R} \mid x = i\}$. (a) $i = 1$ nm; (b) $i = 2$ nm; (c) $i = 3$ nm; (d) $i = 4$ nm. The magnified simulations results for each case clearly indicates the crack widening before splitting into two distinct cracks.

Increasing the tensile stress by using another traction of $\sigma_t = 1.9$ GPa leads to a completely different response in Fig. 4. In comparison to the previous case, the crack tip is formed faster. At $x = 2$ nm in Fig. 4, for the time instant $t = 5$ ps, the peak point of the interface profile is around three times higher than in Fig. 3(b). In addition, the branching happens quicker as well since the distance of bifurcation is smaller in the case of $\sigma_t = 1.5$ GPa. A crack branching angle of 45° followed by a straight extension is observed, which is in good agreement with the literature [126, 130]. In addition, the crack thickness is larger than the initial regularization length ($l = 0.5$ nm) for the simulation results, showing that the crack

tends to grow in its thickness as it propagates towards the right side of the domain. Furthermore, the damage band widening is more visible for this case in comparison with the loading case of $\sigma_t = 1.5\,\text{GPa}$, which is consistent with experiments and other simulations [131].

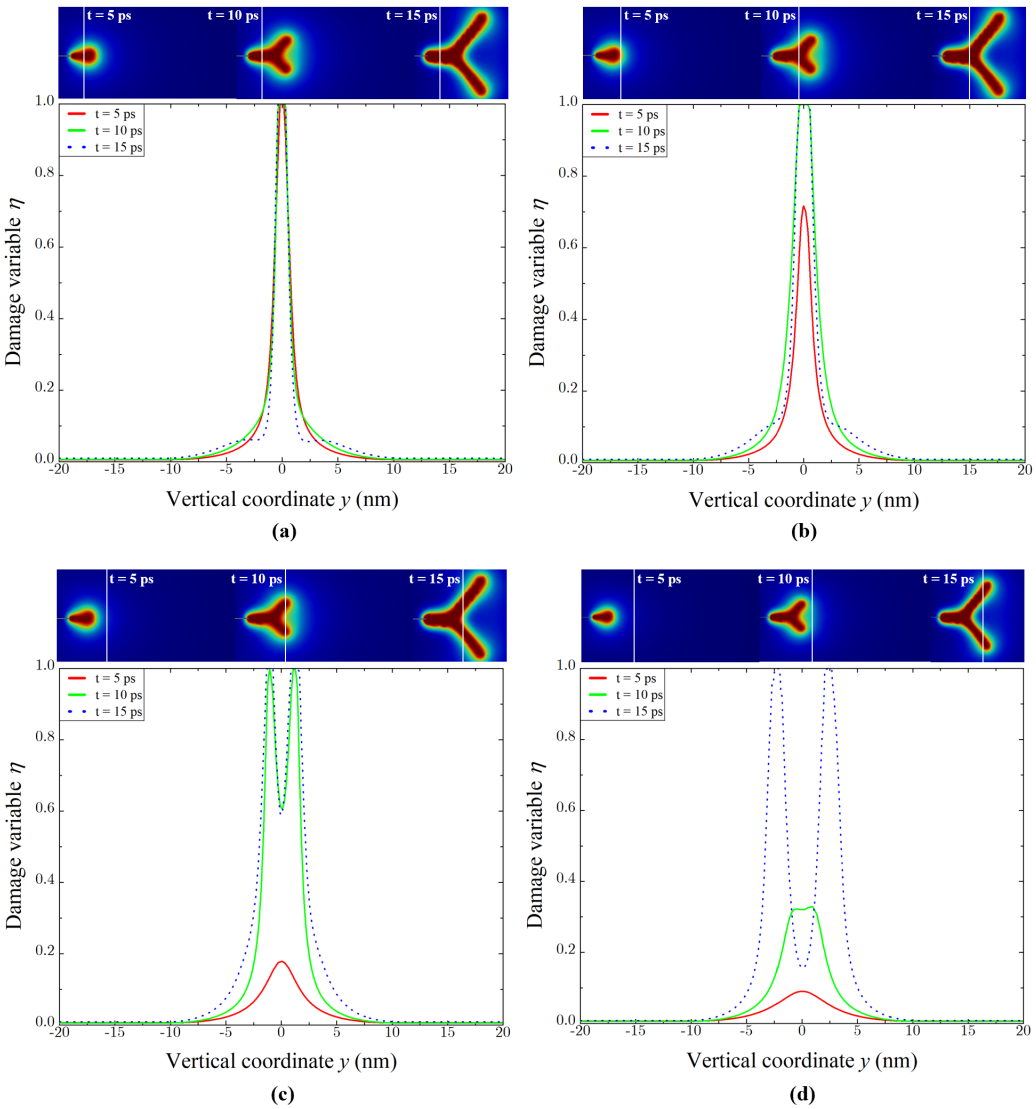

Figure 4: Symmetric damage interfaces under a uniaxial tension stress of 1.9 GPa at different time steps along different vertical slices $\{(x, y) \in \mathbb{R} \mid x = i\}$. (a) $i = 1\,\text{nm}$; (b) $i = 2\,\text{nm}$; (c) $i = 3\,\text{nm}$; (d) $i = 4\,\text{nm}$. The magnified simulations results for each case clearly indicates the crack widening before splitting into two distinct cracks.

In order to better understand the effect of stress magnitude under dynamic loading, the change of crack tip location with time is presented in Fig. 5. In order to determine the crack tip position, we consider the position of (top right) node that has reached $\eta = 0.995$ with

the origin taken at the pre-notch tip (inset of Fig. 5) and by following the upper-branch tip. For the lower loading of $\sigma_t = 1.5\,\mathrm{GPa}$, the evolution is almost linear and no branching is observed.

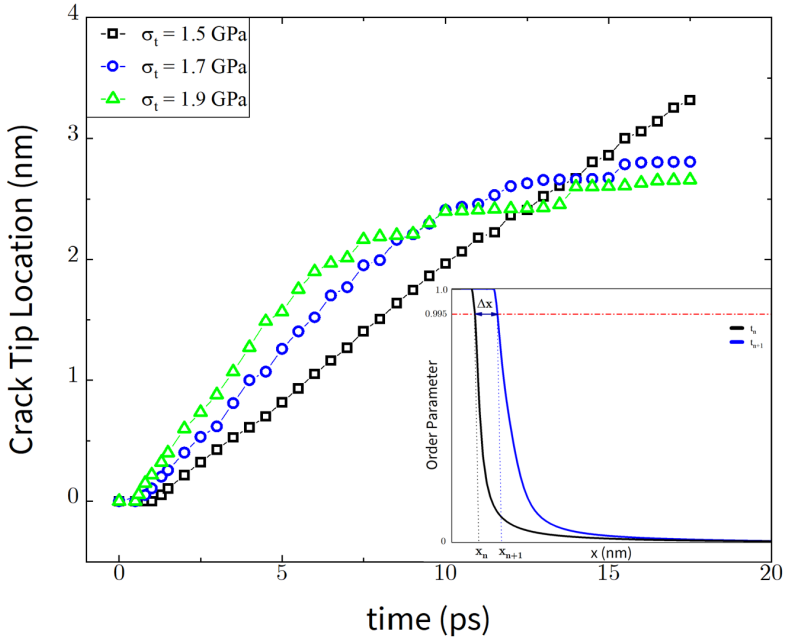

Figure 5: Evolution of crack tip location for different loadings. The inset shows the way of determining the crack tip location at different time steps through the domain's central line in the x direction.

It is also seen that crack tip approaches to a limiting point by increasing the loading. This procedure is quicker up to $t = 7.5\,\mathrm{ps}$ for higher loading scenarios. The initial plateau for different values of the imposed uniaxial stress is related to the time the crack tip forms, which occurs sooner for higher stress values.

4. Conclusion

A robust finite element procedure for solving a coupled system of equilibrium and time-dependent Ginzburg–Landau equations has been motivated by using thermodynamically-sound derivation of governing equations. Use of the variational procedure and thermodynamic consistency of the model ensures that it has a strict relaxational behaviour of the free energy; hence the models are more than a phenomenological description of an interfacial problem as a contrast to the available literature [132]. The dissipation and time scales associated with growth kinetics are also derived and addressed in this manuscript as complementing previous works [64]. The model has been used for studying the evolution of fracture

in anisotropic single crystal boron carbide at finite strains. For the first time, a monolithic strategy has been employed for solving the coupled mechanical equilibrium and order parameters evolution equations under extreme conditions. As a challenge in computational mechanics, nanometer length scale and picosecond time scale have been demonstrated in simulations.

The computational procedures and numerical algorithms are implemented using the open-source platform FEniCS. The present nonlinear finite element code has been developed and used to study the prediction of the dynamic crack path under uniaxial tensile stress loading in single crystal boron carbide. The numerical results for all the problems are in agreement with the available experimental data in the literature. The current contribution opens up new possibilities for multi-scale fracture models. In the future, our finite element based phase-field model can be applied for studies of phase transformations (e.g., amorphization) and interaction between plasticity and fracture under high strain-rate loading. As a next step, the current model could be combined with discrete localized plastic flow (e.g., shear band and dislocation pileups) and thermally-activated mechanisms (e.g., melting) to capture the behavior of brittle materials in laser spall experiments.

5. Data Availability

The authors declare that the main data supporting the findings of this study are available within this article. Extra data are available from the corresponding authors upon reasonable requests.

6. Code Availability

The Python code, generated during the current study, is part of the FEniCS project available at http://www.fenicsproject.org/download, and an example for the computational implementation is available in [133] to be used under the GNU Public license [134].

7. Declaration of Competing Interests

The authors declare no competing financial interests or personal relationships.

8. CRediT Authorship Contributions Statement

B.A developed the model, wrote the code, designed and performed all simulations, analyzed results, and wrote the original draft. B.E.A allocated the computational resources, wrote the code, reviewed and edited the paper. J.D.H supervised the research, acquired funding, reviewed, and edited the paper. All authors discussed the results.

9. Acknowledgements

The authors acknowledge support from Natural Sciences and Engineering Research Council of Canada (NSERC) Discovery Grant 2016-04685 and NSERC DNDPJ 531130-18.

References

[1] B. N. Cox, H. Gao, D. Gross, D. Rittel, Modern topics and challenges in dynamic fracture, Journal of the Mechanics and Physics of Solids 53 (2005) 565–596.

[2] S. Bavdekar, G. Subhash, Failure mechanisms of ceramics under quasi-static and dynamic loads: overview, Handbook of damage mechanics (2022) 579–607.

[3] K. Ravi-Chandar, W. G. Knauss, An experimental investigation into dynamic fracture: Iv. on the interaction of stress waves with propagating cracks, International Journal of Fracture 26 (1984) 189–200.

[4] B. Paliwal, K. Ramesh, Effect of crack growth dynamics on the rate-sensitive behavior of hot-pressed boron carbide, Scripta Materialia 57 (2007) 481–484.

[5] L. Farbaniec, J. Hogan, K. Ramesh, Micromechanisms associated with the dynamic compressive failure of hot-pressed boron carbide, Scripta Materialia 106 (2015) 52–56.

[6] L. Farbaniec, J. Hogan, K. Xie, M. Shaeffer, K. Hemker, K. Ramesh, Damage evolution of hot-pressed boron carbide under confined dynamic compression, International Journal of Impact Engineering 99 (2017) 75–84.

[7] J. LaSalvia, R. Leavy, J. Houskamp, H. Miller, D. MacKenzie, J. Campbell, Ballistic impact damage observations in a hot-pressed boron carbide, in: Ceramic Engineering and Science Proceedings, Vol. 30, 2009, p. 45.

[8] T. Vogler, W. Reinhart, L. Chhabildas, Dynamic behavior of boron carbide, Journal of applied physics 95 (8) (2004) 4173–4183.

[9] T. Holmquist, G. Johnson, Response of boron carbide subjected to high-velocity impact, International Journal of Impact Engineering 35 (8) (2008) 742–752.

[10] D. D. Mallick, K. Ramesh, Dynamic fragmentation of boron carbide using laser-driven flyers, International Journal of Impact Engineering 136 (2020) 103416.

[11] B. M. Koch, H. Li, C. Lo, J. Ligda, J. D. Hogan, Damage accumulation mechanisms during dynamic compressive failure of boron carbide, Journal of the European Ceramic Society (2022).

[12] J. Fineberg, S. P. Gross, M. Marder, H. L. Swinney, Instability in dynamic fracture, Physical Review Letters 67 (4) (1991) 457.

[13] M. Marder, S. Gross, Origin of crack tip instabilities, Journal of the Mechanics and Physics of Solids 43 (1995) 1–48.

[14] F. F. Abraham, J. Q. Broughton, N. Bernstein, E. Kaxiras, Spanning the continuum to quantum length scales in a dynamic simulation of brittle fracture, EPL (Europhysics Letters) 44 (6) (1998) 783.

[15] A. J. Rosakis, O. Samudrala, D. Coker, Cracks Faster than the Shear Wave Speed, Science 284 (1999) 1337–1340.

[16] X. Yan, P. Cao, W. Tao, P. Sharma, H. S. Park, Atomistic modeling at experimental strain rates and timescales, Journal of Physics D: Applied Physics 49 (49) (2016) 493002.

[17] D. Dalmas, C. Guerra, J. Scheibert, D. Bonamy, Damage mechanisms in the dynamic fracture of nominally brittle polymers, International Journal of Fracture 184 (2013) 93–111.

[18] M. Adda-Bedia, R. Arias, M. B. Amar, F. Lund, Generalized griffith criterion for dynamic fracture and the stability of crack motion at high velocities, Physical Review E 60 (1999) 2366.

[19] J. R. Rice, Some studies of crack dynamics, in: Physical Aspects of Fracture, Springer, 2001, pp. 3–11.

[20] A. A. Griffith, Vi. the phenomena of rupture and flow in solids, Philosophical transactions of the royal society of London. Series A, containing papers of a mathematical or physical character 221 (582-593) (1921) 163–198.

[21] L. Scholtès, F.-V. Donzé, Modelling progressive failure in fractured rock masses using a 3d discrete element method, International Journal of Rock Mechanics and Mining Sciences 52 (2012) 18–30.

[22] S. Sinaie, T. D. Ngo, V. P. Nguyen, A discrete element model of concrete for cyclic loading, Computers & structures 196 (2018) 173–185.

[23] N. Moës, J. Dolbow, T. Belytschko, A finite element method for crack growth without remeshing, International journal for numerical methods in engineering 46 (1) (1999) 131–150.

[24] B. Hiriyur, H. Waisman, G. Deodatis, Uncertainty quantification in homogenization of heterogeneous microstructures modeled by xfem, International Journal for Numerical Methods in Engineering 88 (3) (2011) 257–278.

[25] Y. Wang, H. Waisman, From diffuse damage to sharp cohesive cracks: A coupled xfem framework for failure analysis of quasi-brittle materials, Computer Methods in Applied Mechanics and Engineering 299 (2016) 57–89.

[26] X.-P. Xu, A. Needleman, Numerical simulations of fast crack growth in brittle solids, Journal of the Mechanics and Physics of Solids 42 (9) (1994) 1397–1434.

[27] J. J. Remmers, R. de Borst, A. Needleman, A cohesive segments method for the simulation of crack growth, Computational mechanics 31 (1-2) (2003) 69–77.

[28] C. Linder, A. Raina, A strong discontinuity approach on multiple levels to model solids at failure, Computer Methods in Applied Mechanics and Engineering 253 (2013) 558–583.

[29] T. Belytschko, H. Chen, J. Xu, G. Zi, Dynamic crack propagation based on loss of

hyperbolicity and a new discontinuous enrichment, International journal for numerical methods in engineering 58 (12) (2003) 1873–1905.

[30] M. Baydoun, T. Fries, Crack propagation criteria in three dimensions using the xfem and an explicit–implicit crack description, International journal of fracture 178 (1-2) (2012) 51–70.

[31] I. Babuška, J. M. Melenk, The partition of unity method, International journal for numerical methods in engineering 40 (4) (1997) 727–758.

[32] A. Ingraffea, V. Saouma, Numerical model of discrete crack propagation in reinforced and plain concrete, Fracture mechanics of concrete: Structural Application and Numeral Calculation (1985) 171–225.

[33] D. Sutula, P. Kerfriden, T. Van Dam, S. P. Bordas, Minimum energy multiple crack propagation. part i: Theory and state of the art review, Engineering Fracture Mechanics 191 (2018) 205–224.

[34] K. Pham, J.-J. Marigo, Approche variationnelle de l'endommagement: Ii. les modčles ą gradient, Comptes Rendus Mécanique 338 (4) (2010) 199–206.

[35] O. Aslan, N. Cordero, A. Gaubert, S. Forest, Micromorphic approach to single crystal plasticity and damage, International Journal of Engineering Science 49 (12) (2011) 1311–1325.

[36] V. Hakim, A. Karma, Laws of crack motion and phase-field models of fracture, Journal of the Mechanics and Physics of Solids 57 (2) (2009) 342–368.

[37] F. Aldakheel, B. Hudobivnik, P. Wriggers, Virtual elements for finite thermo-plasticity problems, Computational Mechanics 64 (5) (2019) 1347–1360.

[38] A. Karma, D. A. Kessler, H. Levine, Phase-field model of mode iii dynamic fracture, Physical Review Letters 87 (4) (2001) 045501.

[39] M. Hofacker, C. Miehe, Continuum phase field modeling of dynamic fracture: variational principles and staggered fe implementation, International Journal of Fracture 178 (1-2) (2012) 113–129.

[40] M. J. Borden, C. V. Verhoosel, M. A. Scott, T. J. Hughes, C. M. Landis, A phase-field description of dynamic brittle fracture, Computer Methods in Applied Mechanics and Engineering 217 (2012) 77–95.

[41] J.-H. Song, H. Wang, T. Belytschko, A comparative study on finite element methods for dynamic fracture, Computational Mechanics 42 (2) (2008) 239–250.

[42] P.-E. Bernard, N. Moës, N. Chevaugeon, Damage growth modeling using the thick level set (tls) approach: Efficient discretization for quasi-static loadings, Computer Methods in Applied Mechanics and Engineering 233 (2012) 11–27.

[43] S. Mariani, U. Perego, Extended finite element method for quasi-brittle fracture, International Journal for Numerical Methods in Engineering 58 (1) (2003) 103–126.

[44] M. Javanbakht, M. S. Ghaedi, E. Barchiesi, A. Ciallella, The effect of a pre-existing nanovoid on martensite formation and interface propagation: a phase field study, Mathematics and Mechanics of Solids 26 (1) (2021) 90–109.

[45] J. Slutsker, K. Thornton, A. Roytburd, J. A. Warren, G. B. McFadden, Phase field modeling of solidification under stress, Physical Review B 74 (1) (2006) 014103.

[46] C. Albrecht, A. Hunter, A. Kumar, I. Beyerlein, A phase field model for dislocations in hexagonal close packed crystals, Journal of the Mechanics and Physics of Solids 137 (2020) 103823.

[47] B. Amirian, H. Jafarzadeh, B. E. Abali, A. Reali, J. D. Hogan, Phase-field approach to evolution and interaction of twins in single crystal magnesium, Computational Mechanics (2022).

[48] B. Bourdin, G. A. Francfort, J.-J. Marigo, Numerical experiments in revisited brittle fracture, Journal of the Mechanics and Physics of Solids 48 (4) (2000) 797–826.

[49] B. Bourdin, G. A. Francfort, J.-J. Marigo, The variational approach to fracture, Journal of elasticity 91 (1-3) (2008) 5–148.

[50] V. I. Levitas, H. Jafarzadeh, G. H. Farrahi, M. Javanbakht, Thermodynamically consistent and scale-dependent phase field approach for crack propagation allowing for surface stresses, International Journal of Plasticity 111 (2018) 1–35.

[51] H. Jafarzadeh, V. I. Levitas, G. H. Farrahi, M. Javanbakht, Phase field approach for nanoscale interactions between crack propagation and phase transformation, Nanoscale 11 (46) (2019) 22243–22247.

[52] C. Kuhn, R. Müller, A continuum phase field model for fracture, Engineering Fracture Mechanics 77 (18) (2010) 3625–3634.

[53] L. Placidi, E. Barchiesi, A. Misra, U. Andreaus, Variational methods in continuum damage and fracture mechanics, Encyclopedia of continuum mechanics (2020) 2634–2643.

[54] J. M. Sargado, E. Keilegavlen, I. Berre, J. M. Nordbotten, High-accuracy phase-field models for brittle fracture based on a new family of degradation functions, Journal of the Mechanics and Physics of Solids 111 (2018) 458–489.

[55] E. Eid, R. Seghir, J. Réthoré, Multiscale analysis of brittle failure in heterogeneous materials, Journal of the Mechanics and Physics of Solids 146 (2021) 104204.

[56] M. A. Msekh, J. M. Sargado, M. Jamshidian, P. M. Areias, T. Rabczuk, Abaqus implementation of phase-field model for brittle fracture, Computational Materials Science 96 (2015) 472–484.

[57] A. Ruffini, A. Finel, Phase-field model coupling cracks and dislocations at finite strain, Acta Materialia 92 (2015) 197–208.

[58] N. Mozaffari, G. Z. Voyiadjis, Coupled gradient damage–viscoplasticty model for ductile materials: Phase field approach, International Journal of Plasticity 83 (2016) 55–73.

[59] R. Schmitt, C. Kuhn, R. Skorupski, M. Smaga, D. Eifler, R. Müller, A combined phase field approach for martensitic transformations and damage, Archive of Applied Mechanics 85 (9-10) (2015) 1459–1468.

[60] Thermodynamically-consistent derivation and computation of twinning and fracture in brittle materials by means of phase-field approaches in the finite element method, International Journal of Solids and Structures 252 (2022) 111789.

[61] O. Gültekin, H. Dal, G. A. Holzapfel, A phase-field approach to model fracture of arterial walls: theory and finite element analysis, Computer methods in applied mechanics and engineering 312 (2016) 542–566.

[62] J.-Y. Wu, V. P. Nguyen, C. T. Nguyen, D. Sutula, S. Bordas, S. Sinaie, Phase field modeling of fracture, Advances in applied mechancis: multi-scale theory and computation 52 (2018).

[63] A. C. Hansen-Dörr, F. Dammaß, R. de Borst, M. Kästner, Phase-field modeling of crack branching and deflection in heterogeneous media, Engineering Fracture Mechanics 232 (2020) 107004.

[64] J. Clayton, J. Knap, Phase field modeling and simulation of coupled fracture and twinning in single crystals and polycrystals, Computer Methods in Applied Mechanics and Engineering 312 (2016) 447–467.

[65] A. C. Hansen-Dörr, R. de Borst, P. Hennig, M. Kästner, Phase-field modelling of interface failure in brittle materials, Computer Methods in Applied Mechanics and Engineering 346 (2019) 25–42.

[66] A. Emdadi, M. A. Zaeem, Phase-field modeling of crack propagation in polycrystalline materials, Computational Materials Science 186 (2021) 110057.

[67] D. Timofeev, E. Barchiesi, A. Misra, L. Placidi, Hemivariational continuum approach for granular solids with damage-induced anisotropy evolution, Mathematics and Mechanics of Solids 26 (5) (2021) 738–770.

[68] L. Landau, E. Lifshitz, Statistical physics. vol. 5 . pergamon press. oxford-new york (1980).

[69] I. Aranson, V. Kalatsky, V. Vinokur, Continuum field description of crack propagation, Physical review letters 85 (1) (2000) 118.

[70] L. Hai, J. Li, A rate-dependent phase-field framework for the dynamic failure of quasi-brittle materials, Engineering Fracture Mechanics 252 (2021) 107847.

[71] C. Miehe, F. Welschinger, M. Hofacker, Thermodynamically consistent phase-field

models of fracture: Variational principles and multi-field fe implementations, International journal for numerical methods in engineering 83 (10) (2010) 1273–1311.

[72] C. Miehe, M. Hofacker, F. Welschinger, A phase field model for rate-independent crack propagation: Robust algorithmic implementation based on operator splits, Computer Methods in Applied Mechanics and Engineering 199 (45-48) (2010) 2765–2778.

[73] N. Singh, C. Verhoosel, R. De Borst, E. Van Brummelen, A fracture-controlled path-following technique for phase-field modeling of brittle fracture, Finite Elements in Analysis and Design 113 (2016) 14–29.

[74] T. Heister, M. F. Wheeler, T. Wick, A primal-dual active set method and predictor-corrector mesh adaptivity for computing fracture propagation using a phase-field approach, Computer Methods in Applied Mechanics and Engineering 290 (2015) 466–495.

[75] M. Ambati, T. Gerasimov, L. De Lorenzis, A review on phase-field models of brittle fracture and a new fast hybrid formulation, Computational Mechanics 55 (2) (2015) 383–405.

[76] V. I. Levitas, D. L. Preston, Thermomechanical lattice instability and phase field theory of martensitic phase transformations, twinning and dislocations at large strains, Physics Letters A 343 (1-3) (2005) 32–39.

[77] N. Gorbushin, V. A. Eremeyev, G. Mishuris, On stress singularity near the tip of a crack with surface stresses, International Journal of Engineering Science 146 (2020) 103183.

[78] M. Alnæs, J. Blechta, J. Hake, A. Johansson, B. Kehlet, A. Logg, C. Richardson, J. Ring, M. E. Rognes, G. N. Wells, The fenics project version 1.5, Archive of Numerical Software 3 (100) (2015).

[79] B. E. Abali, Computational Reality: Solving Nonlinear and Coupled Problems in Continuum Mechanics, Springer Singapore, 2017.

[80] N. Provatas, K. Elder, Phase-field methods in materials science and engineering, John Wiley & Sons, 2011.

[81] F. A. Denli, O. Gültekin, G. A. Holzapfel, H. Dal, A phase-field model for fracture of unidirectional fiber-reinforced polymer matrix composites, Computational Mechanics 65 (4) (2020) 1149–1166.

[82] M. Kästner, P. Metsch, R. De Borst, Isogeometric analysis of the cahn–hilliard equation–a convergence study, Journal of Computational Physics 305 (2016) 360–371.

[83] A. C. Hansen-Dörr, J. Brummund, M. Kästner, Phase-field modeling of fracture in heterogeneous materials: jump conditions, convergence and crack propagation, Archive of Applied Mechanics 91 (2) (2021) 579–596.

[84] C. Miehe, F. Aldakheel, A. Raina, Phase field modeling of ductile fracture at finite strains: A variational gradient-extended plasticity-damage theory, International Journal of Plasticity 84 (2016) 1–32.

[85] S. Yang, F. Aldakheel, A. Caggiano, P. Wriggers, E. Koenders, A review on cementitious self-healing and the potential of phase-field methods for modeling crack-closing and fracture recovery, Materials 13 (22) (2020) 5265.

[86] P. Karandikar, G. Evans, S. Wong, M. Aghajanian, M. Sennett, A review of ceramics for armor applications, Advances in Ceramic Armor IV 29 (2009) 163–175.

[87] G. Samsonov, V. Matkovich, P. Hagenmuller, T. Lundstrom, Boron and refractory borides, Springer Science & Business Media, 2012.

[88] C. Subramanian, A. Suri, T. Murthy, Development of boron-based materials for nuclear applications, Barc Newsletter 313 (2010) 14.

[89] F. Thevenot, Boron carbide—a comprehensive review, Journal of the European Ceramic society 6 (4) (1990) 205–225.

[90] Y. Li, Y. Zhao, W. Liu, Z. Zhang, R. Vogt, E. Lavernia, J. Schoenung, Deformation twinning in boron carbide particles within nanostructured al 5083/b4c metal matrix composites, Philosophical Magazine 90 (6) (2010) 783–792.

[91] Q. An, W. A. Goddard III, T. Cheng, Atomistic explanation of shear-induced amorphous band formation in boron carbide, Physical review letters 113 (9) (2014) 095501.

[92] V. Eremeyev, F. Fischer, On the phase transitions in deformable solids, Journal of Applied Mathematics and Mechanics/Zeitschrift für Angewandte Mathematik und Mechanik 90 (7-8) (2010) 535–536.

[93] Q. An, W. A. Goddard III, Atomistic origin of brittle failure of boron carbide from large-scale reactive dynamics simulations: Suggestions toward improved ductility, Physical review letters 115 (10) (2015) 105501.

[94] S. Zhao, B. Kad, B. A. Remington, J. C. LaSalvia, C. E. Wehrenberg, K. D. Behler, M. A. Meyers, Directional amorphization of boron carbide subjected to laser shock compression, Proceedings of the National Academy of Sciences 113 (43) (2016) 12088–12093.

[95] X. Yan, Z. Tang, L. Zhang, J. Guo, C. Jin, Y. Zhang, T. Goto, J. McCauley, M. Chen, Depressurization amorphization of single-crystal boron carbide, Physical review letters 102 (7) (2009) 075505.

[96] G. Fanchini, J. W. McCauley, M. Chhowalla, Behavior of disordered boron carbide under stress, Physical review letters 97 (3) (2006) 035502.

[97] D. E. Taylor, J. W. McCauley, T. Wright, The effects of stoichiometry on the mechanical properties of icosahedral boron carbide under loading, Journal of Physics: Condensed Matter 24 (50) (2012) 505402.

[98] J. Clayton, Dynamic plasticity and fracture in high density polycrystals: constitutive modeling and numerical simulation, Journal of the Mechanics and Physics of Solids 53 (2) (2005) 261–301.

[99] C. A. H. Padilla, B. Markert, A coupled ductile fracture phase-field model for crystal plasticity, Continuum Mechanics and Thermodynamics 29 (4) (2017) 1017–1026.

[100] J. W. Cahn, J. E. Hilliard, Free energy of a nonuniform system. i. interfacial free energy, The Journal of chemical physics 28 (2) (1958) 258–267.

[101] S. M. Allen, J. W. Cahn, A microscopic theory for antiphase boundary motion and its application to antiphase domain coarsening, Acta metallurgica 27 (6) (1979) 1085–1095.

[102] V. I. Levitas, D. L. Preston, Three-dimensional landau theory for multivariant stress-induced martensitic phase transformations. i. austenite martensite, Physical review B 66 (13) (2002) 134206.

[103] I. Müller, W. H. Müller, Fundamentals of thermodynamics and applications: with historical annotations and many citations from Avogadro to Zermelo, Springer Science & Business Media, 2009.

[104] V. I. Levitas, Phase field approach to martensitic phase transformations with large strains and interface stresses, Journal of the Mechanics and Physics of Solids 70 (2014) 154–189.

[105] G. De With, High temperature fracture of boron carbide: experiments and simple theoretical models, Journal of materials science 19 (1984) 457–466.

[106] G. A. Francfort, J.-J. Marigo, Revisiting brittle fracture as an energy minimization problem, Journal of the Mechanics and Physics of Solids 46 (8) (1998) 1319–1342.

[107] P. Farrell, C. Maurini, Linear and nonlinear solvers for variational phase-field models of brittle fracture, International Journal for Numerical Methods in Engineering 109 (5) (2017) 648–667.

[108] G. Oleinik, T. Ostapchuk, Effect of pores on the cleavage of twinned boron carbide crystals, Powder Metallurgy and Metal Ceramics 34 (9) (1996) 500–504.

[109] J. Clayton, Finsler-geometric continuum mechanics and the micromechanics of fracture in crystals, Journal of Micromechanics and Molecular Physics 1 (03n04) (2016) 1640003.

[110] G. N. Greaves, A. Greer, R. S. Lakes, T. Rouxel, Poisson's ratio and modern materials, Nature materials 10 (11) (2011) 823–837.

[111] T. I. Zohdi, Finite element primer for beginners, Springer, 2018.

[112] M. S. Alnæs, K.-A. Mardal, On the efficiency of symbolic computations combined with code generation for finite element methods, ACM Transactions on Mathematical Software (TOMS) 37 (1) (2010) 1–26.

[113] M. S. Alnæs, K.-A. Mardal, Syfi and sfc: Symbolic finite elements and form compilation, in: Automated Solution of Differential Equations by the Finite Element Method, Springer, 2012, pp. 273–282.

[114] A. Logg, G. N. Wells, Dolfin: Automated finite element computing, ACM Transactions on Mathematical Software (TOMS) 37 (2) (2010) 1–28.

[115] B. E. Abali, A. Klunker, E. Barchiesi, L. Placidi, A novel phase-field approach to brittle damage mechanics of gradient metamaterials combining action formalism and history variable, ZAMM-Journal of Applied Mathematics and Mechanics/Zeitschrift für Angewandte Mathematik und Mechanik 101 (9) (2021) e202000289.

[116] E. Barchiesi, H. Yang, C. Tran, L. Placidi, W. H. Müller, Computation of brittle fracture propagation in strain gradient materials by the fenics library, Mathematics and Mechanics of Solids 26 (3) (2021) 325–340.

[117] R. G. Tangella, P. Kumbhar, R. K. Annabattula, Hybrid phase field modelling of dynamic brittle fracture and implementation in fenics, Composite Materials for Extreme Loading (2022) 15–24.

[118] P. Cheng, H. Zhu, Y. Zhang, Y. Jiao, J. Fish, Coupled thermo-hydro-mechanical-phase field modeling for fire-induced spalling in concrete, Computer Methods in Applied Mechanics and Engineering 389 (2022) 114327.

[119] Y. Lu, T. Helfer, B. Bary, O. Fandeur, An efficient and robust staggered algorithm applied to the quasi-static description of brittle fracture by a phase-field approach, Computer Methods in Applied Mechanics and Engineering 370 (2020) 113218.

[120] K. B. Ølgaard, A. Logg, G. N. Wells, Automated code generation for discontinuous galerkin methods, SIAM Journal on Scientific Computing 31 (2) (2009) 849–864.

[121] K. B. Ølgaard, G. N. Wells, Optimizations for quadrature representations of finite element tensors through automated code generation, ACM Transactions on Mathematical Software (TOMS) 37 (1) (2010) 1–23.

[122] L. J. Slutsky, C. W. Garland, Elastic constants of magnesium from 4.2°K to 300°K, Phys. Rev. 107 (1957) 972–976.

[123] D. Taylor, T. Wright, J. McCauley, First principles calculation of stress induced amorphization in armor ceramics, Tech. rep., Army Research Lab Aberdeen Proving Ground MD (2011).

[124] J. Clayton, Towards a nonlinear elastic representation of finite compression and instability of boron carbide ceramic, Philosophical Magazine 92 (23) (2012) 2860–2893.

[125] T. D. Beaudet, J. R. Smith, J. W. Adams, Surface energy and relaxation in boron carbide (1011) from first principles, Solid State Communications 219 (2015) 43–47.

[126] E. Katzav, M. Adda-Bedia, R. Arias, Theory of dynamic crack branching in brittle materials, International Journal of Fracture 143 (3) (2007) 245–271.

[127] J. Fineberg, S. P. Gross, M. Marder, H. L. Swinney, Instability in the propagation of fast cracks, Physical Review B 45 (10) (1992) 5146.

[128] J. Bleyer, R. Alessi, Phase-field modeling of anisotropic brittle fracture including several damage mechanisms, Computer Methods in Applied Mechanics and Engineering 336 (2018) 213–236.

[129] C. Hesch, K. Weinberg, Thermodynamically consistent algorithms for a finite-deformation phase-field approach to fracture, International Journal for Numerical Methods in Engineering 99 (12) (2014) 906–924.

[130] G. D. Quinn, On crack branching angles in glasses and ceramics, Journal of the European Ceramic Society 40 (14) (2020) 4711–4721.

[131] F. Bobaru, G. Zhang, Why do cracks branch? a peridynamic investigation of dynamic brittle fracture, International Journal of Fracture 196 (1) (2015) 59–98.

[132] Z. Guo, P. Lin, A thermodynamically consistent phase-field model for two-phase flows with thermocapillary effects, Journal of Fluid Mechanics 766 (2015) 226–271.

[133] B. E. Abali, Supply code for computations, http://bilenemek.abali.org/ (2020).

[134] GNU Public, Gnu general public license, http://www.gnu.org/copyleft/gpl.html.